Journal of the Korean Physical Society, Vol. 56, No. 3, March 2010, pp. 851∼855

Mechanism of Embedded Micro/Nano Channel Formation for a Negative-tone Photoresist by Moving Mask Lithography

Sang-Kon Kim,* Hye-Keun Oh, Young-Dae Jung and Ilsin An
Department of Applied Physics, Hanyang University, Ansan 426-791

(Received 9 March 2009, in final form 21 January 2010)

Photoresist lithography has been applied in MEMS (micro electro mechanical systems). A flexible 3D (three-dimensional) micro/nano fabrication technique and its process simulation tool are required for 3D MEMS. This paper presents an UV (ultraviolet) lithography process simulation for the formation of an embedded micro/nano fluidic channel in a negative-tone photoresist. For this purpose, the moving-mask technology is modeled. The simulation algorithm of the nano-lithography is applied for the micro-lithography. The validity of the simulation for the proposed 3D microstructuring is successfully confirmed by a comparison between the experimental and the simulated results. Hence, modeling and simulation for the formation of various patterns of micro/nano fluidic channels in a negative-tone photoresist can be used to provide the photoresist characteristics and to optimize the lithography process conditions.

PACS numbers: 85.40.Hp, 78.20.Bh, 07.10.Cm, 81.16.Nd, 85.40.Bh
Keywords: Lithography, Lithography simulation, Negative resist, Chemically amplified resist, Multi-exposures, Inverse lithography, Embedded fluidic channels, MEMS.
DOI: 10.3938/jkps.56.851

I. INTRODUCTION

Micro/nano systems can manipulate information with light, diagnose the body from the inside, or assemble parts of operating individual atoms and molecules by integrating functional elements in different domains, such as mechanics, electronics, chemistry, optics, and biotechnology. Application of 3D (three-dimensional) photoresist microstructures on substrate surfaces has been of great interest because these microstructures are applicable to various MEMS (micro-electro-mechanical system) devices [1]. For micro/nano fluids, the micro/nano channels can be used for material/bio devices to pass (or filter) the desired chemical or biological elements. From the idea of a nano/microstructure, the modeling and the simulation of lithography processes can reduce manufacture cost and time at the design step, the fabrication step, the test step, and the packaging step. For the process of micro/nano fluidic channel formation, the multi-step fabrication composed of lithography, etch, and mold processes is more complicated and expensive than the single-step fabrication compared of moving-mask lithography. Moving-mask lithography with a single exposure step can realize micro/nano fluidic channels with a semi-arbitrary cross-sectional shape. Moving-mask lithography can control the sidewall angle of the pattern by varying the mask-movement trajectory [2,3].

*E-mail: sangkona@hotmail.com; http://www.sangkon.info

A lithography process simulation is required to develop and verify process conditions in a thick/thin and negative photoresist. Hirai *et al* (Ref. 2) proposed a macro-scale simulation in a positive tone resist and used a photoresist dissolution rate function to consider the photoresist dissolution vector in the development process by fitting the experimental profile data with the develop time. However, this paper describes both macro- and nano-scale simulations and models with optical, chemical, and mechanical phenomena during moving-mask lithography. In this paper, the embedded micro/nano fluidic channels formed in a negative chemically amplified resist (CAR) by moving-mask UV (ultraviolet) lithography are modeled and simulated by using full lithography processes, which include exposure, post exposure process (PEB), and development.

II. MOVING-MASK LITHOGRAPHY

Figure 1 shows a comparison of the multi-step method with moving-mask lithography for the fabrication of embedded micro/nano fluidic channels. The multi-step method is composed of lithography, etch, and mold. This method can make limited shapes. Hence, the multi-step method is more complicated and expensive than the moving-mask lithography. For the microchannels' sidewall and ceiling, the deposited dose depends on the mask-movement trajectory of the line and space (L/S) mask

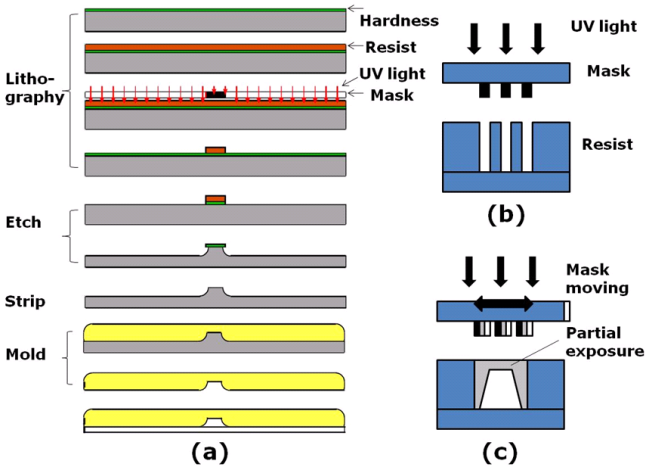

Fig. 1. Schematic drawing of (a) a multi-step method and (c) the moving-mask lithography for manufacturing embedded micro/nano channel and of (b) the normal lithography for the formation of line and space patterns.

pattern. The sidewall angle increases according for a longer mask-movement range. Optimization of the photoresist characteristics and the lithography process conditions is expected to enable the fabrication of various micro/nano embedded fluidic channels.

Figure 2 shows a simple schematic for the mechanism of the macro/nano embedded channel formation according to the mask's moving range ($R_1 < R_2 < R_3$ in Fig. 2). The deposited dose and the pattern profile on a negative photoresist correspond to the three kinds of the mask movement trajectories. When the mask moves in the range of pitch size, a fine embedded channel is formed from the non-crosslink region inside a negative resist. Hence, the limited movements of the mask cause the 3-D macro/nano embedded channels. The deposited doses of the nano/macro embedded channels' sidewall and ceiling depend on variations in the mask-movement trajectory. The velocity and the movement range of the mask can be used to control the sidewall angle, width, and height of the channels.

Figure 3 shows the distributed dose deposited inside a resist at the initial time and at time τ according to Fig. 2. When the mask is moved a distance τ in Fig. 3, the function E(x) of the deposited dose on the resist at position x is

$$E(x)_\tau = M(x-\tau)F(\tau) \rightarrow E(x) = \int M(x-\tau)F(\tau)d\tau \ , \tag{1}$$

where $E(x)_\tau$ denotes the deposited dose on the resist when the mask is positioned at $x = \tau$, $M(x-\tau)$ is a function defined by one of two values, which are 0 for an opaque mask and 1 for a transparent mask, and $F(\tau)$ is a function of the deposited dose at the position where the mask is moved. $E(x)$, $M(x)$, and $F(\tau)$ are transformed to $E(f)$, $M(f)$, and $F(f)$ with the convolution theorem by using Fourier transformations:

$$E(f) = M(f)F(f) \rightarrow F(f) = E(f)/M(f) \tag{2}$$

By applying the inverse Fourier transformation to Eq. (2), the pattern function of the mask movement, $F(\tau)$, is derived. This concept makes it possible to derive the mask movement pattern mathematically, which realizes the distributed dose corresponding to the target shape without trial and error. In this research, the suggested patterns are line and space (L/S) patterns. The proposed movement of the mask is distinguished from the movement of the mask in a scanner. According to Fig. 2, when the movement range of mask is the L/S pitch size, a fine embedded fluidic channel is formed.

III. NEGATIVE LITHOGRAPHY SIMULATION

In general, the chemically amplified negative-type resist is composed of polymer, a photo/radio-sensitive compound called a photo acid generator (PAG) and a cross-linker. For the mechanism of the lithography process in a negative-tone resist, during the exposure process, the negative CAR is irradiated by using deep-ultra violet (DUV) radiation, so that the PAG generates acid. During PEB, the acid catalyzes cross-linking reactions among the polymer chains directly or through the cross-linker. The cross-linking leads to the formation of polymer clusters and finally to a gel state, which is considered insoluble to the developer. During the development process, the developer dissolves single and uncross-linked polymer chains. As a result, the region of the resist film with the absorbed radiation becomes less soluble than the neighboring regions with the non-absorbed radiation. The neighboring regions dissolve faster and reveal the surface of the substrate. Hence, for the exposure process, exposing a CAR resist to DUV light generates both acid from a PAG and a cross-linking reaction caused by the photon energy:

$$\frac{d[PAG]}{dt} = -C \cdot [PAG] \cdot I \ , \tag{3}$$

$$\begin{aligned} [H^+]_t &= [PAG]_{t=0} - [PAG]_t \\ &= [PAG]_{t=0}(1 - e^{-CE}) \ , \end{aligned} \tag{4}$$

$$\frac{d[S_{ci}]}{dt} = -k_{photo} \cdot [S_{ci}] \cdot I \ , \tag{5}$$

where PAG is the photo-acid generator, E is the exposure dose, C is a Dill's parameter, t is the exposure time, k_{photo} is the cross-linking reaction constant for the cross-linking reaction attributable to the photon energy generated by exposure, I is the intensity of incident light, and $[S_{ci}]$ is the normalized concentration of the reactive groups in the cross-linking agent. During PEB, the

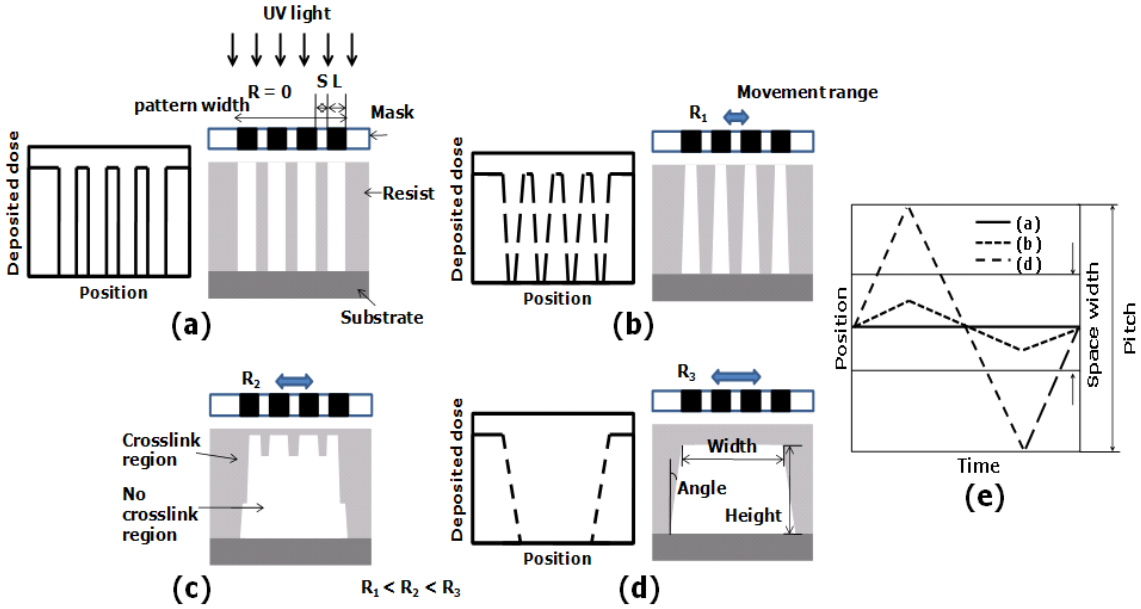

Fig. 2. Schematic of the mechanism for the formation of embedded macro/nano channels according to the range of mask movement at a velocity: (a) R = 0, (b) R = R_1, (c) R = R_2, and (d) R = R_3, where R is the range of mask movement and $R_1 < R_2 < R_3$. For a negative resist, (a), (b), and (d) pattern profiles correspond to the three kinds of (a), (b), and (d) of the mask movement trajectories in Fig. 2(e).

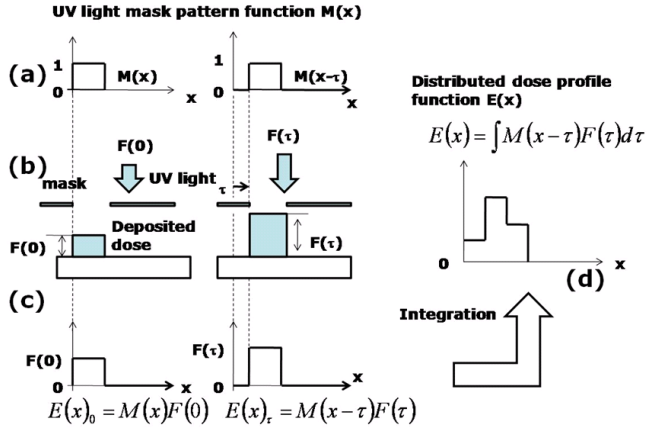

Fig. 3. Exposure step of moving-mask lithography at the initial time and the time τ: (a) mask moving, (b) distributed dose on the mask at the position when the mask has moved by a distance τ, (c) deposited dose inside the resist at position x, and (d) integrated distributed dose profile deposited at the resist surface.

photo-generated acid catalyzes a thermally induced reaction:

$$\frac{d[H^+]}{dt'} = -k_{loss}\cdot[H^+] - k_{quench}\cdot[A]\cdot[B] + \nabla\cdot(D_{acid}\nabla[H^+]) \ , \quad (6)$$

$$\frac{d[B]}{dt'} = -k_{quench}\cdot[H^+]^m\cdot[B] \ , \quad (7)$$

$$\frac{d[S_{ci}]}{dt'} = -k_{ci}\cdot[H^+]^m\cdot[S_{ci}] \ , \quad (8)$$

where t' is the PEB time (sec), $[H^+]^m$ is the acid concentration, [B] is the base quencher, D_{acid} is the diffusion constant of the acid, m is the order of the cross-linking reaction, k_{ci} is the cross-linking reaction constant, k_{quench} is the rate of acid neutralization, and k_{loss} is a constant corresponding to the deactivation of the acid [4,5].

IV. SIMULATION AND ANALYSIS

Figure 4 shows the distributed dose deposited over a positive-tone resist by applying the inverse approach of Fig. 3. The pattern function, $F(\tau)$, of the mask's movement in Fig. 4(f) is derived by applying the fast Fourier transformation (FFT) and the inverse FFT. However, the inverse approach requires a correction to yield a successful matching of simulation results to experimental results. The correction is performed in the convection step from the function $T(x)$ of the target shape to the function $E(x)$ of the distributed dose. The function $T(x)$ in Fig. 4 is the relation of the resist thickness's reduction to dose. The dependence of the resist thickness's reduction on the deposited dose can be obtained through the normal exposure without the mask movement. The inverse approach with the conversion step can provide not only a suitable mask movement pattern but also the optimal mask [6].

If a negative resist is composed of a polymer resin and a photoacid generator (PAG), the PAG generates acid (H^+) by acting with ultraviolet light ($PAG + h\nu \rightarrow H^+$). The exposure dose is distributed over and is deposited

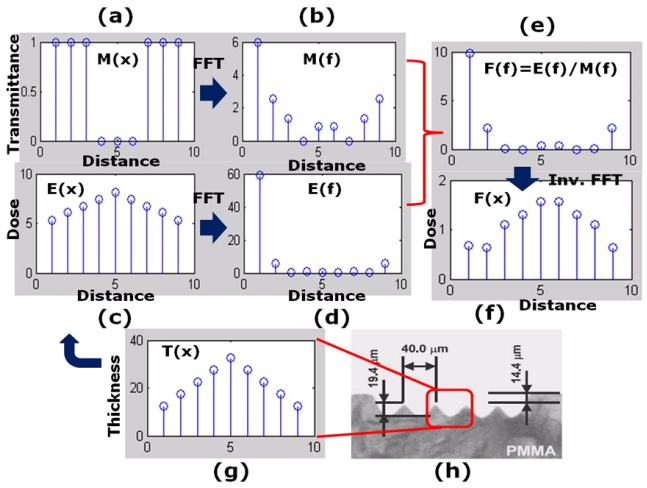

Fig. 4. Inverse approach of the distributed dose profile deposited over the resist surface for a positive-tone resist: (a) mask function $M(x)$, (b) Fourier transformation $M(f)$ of $M(x)$, (c) the deposited dose $E(x)$ on the resist surface at position x, (d) Fourier transformation $E(f)$ of $E(x)$, (e) Fourier transformation $F(f)$, (f) distributed dose $F(\tau)$ on the mask according to the position when the mask is moved by a distance τ, (g) target shape function $T(x)$, and (h) cross-section of the fabricated microstructure. 'FFT' in the graph legends between (a) and (b) indicates 'Fast Fourier Transformation,' 'Inv. FFT' in the graph legends between (e) and (f) indicates 'Inverse Fast Fourier Transformation.

into the resist by the moving mask. During PEB, the photo-generated acid changes the blocked resin into deblocked resin (H^+ + *Blocked Resin* → H^+ + *Deblocked Resin*). After the development process, an embedded fluidic channel has been formed [7]. For the moving-mask lithography, various profile shapes correspond to various aerial images. Hence, the aerial image of a normal lithography simulator is modified into the deposited dose into the resist of the moving-mask lithography by using the inverse approach, which includes a conversion step from the target shape function. The simulation profiles of the moving-mask lithography are calculated by using the modified aerial images as input data to the developed lithography simulator.

Figure 5 shows the simulation results of negative CAR processes for 75.5-nm line and space (L/S) pattern formation. Simulation results of a negative CAR are the aerial image of the illumination calculation in Fig. 5(a), the PAG concentration of Eq. (3) after exposure process in Fig. 5(b), the cross-linked polymer concentration of Eq. (8) after PEB corresponding to the de-protected inhibitor concentration in a positive process in Fig. 5(c), the dissolution rate concentration of Mack's model for development in Fig. 5(d), and a pattern profile of the ray trace algorithm in Figs. 5(f) and (h). The simulation results in Figs. 5(f) and (h) are in good agreement with the experimental results for a 75.5-nm L/S pattern profile in Fig. 5(e) and for a 20-μm L/S pattern profile

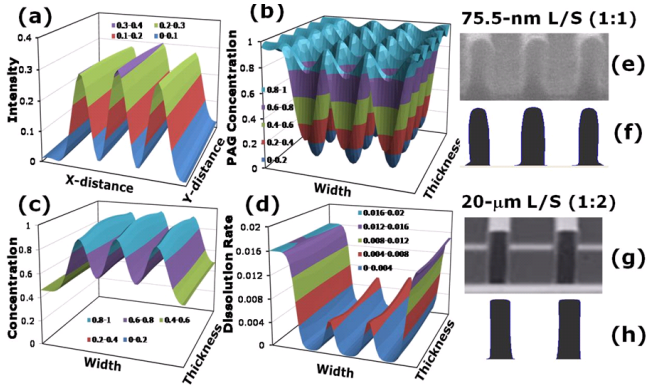

Fig. 5. Comparison of the simulation with experimental results in negative CAR processes for the micro/nano L/S pattern formation: (a) aerial image, (b) PAG concentration, (c) cross-linked polymer concentration, (d) development rate concentration, (e) and (g) experimental results [8,9], and (f) and (h) simulation results for a 75.5-nm line and space (L/S = 1:1) pattern and a 20-μm (L/S = 1:2) pattern.

in Fig. 5(g), respectively. For the 75.5-nm (L/S = 1:1) pattern formations in Figs. 5(e) and (f), experiment conditions corresponding to the simulation conditions were a 193-nm wavelength, a resist of 90-nm ARC thickness, and a 210-nm resist thickness, a 6% attenuated phase-shifting mask, a 0.75 numerical aperture (NA), an annular illumination with an outer 0.89 σ and an inner 0.55 σ, a 26.2-mJ/cm^2 exposure, a post-apply bake (PAB) at 105 °C for 60 sec, a PEB at 105 °C for 60 sec, and development for 60 sec [8]. For a 20-μm (L/S = 1:2) pattern formation, experimental conditions corresponding to the simulation conditions were a 365-nm wavelength, a 90-nm ARC thickness, a 74-μm resist thickness, a 0.63 NA, a convention illumination with 0.6 σ, a 150-mJ/cm^2 exposure, a 1stPAB at 65 °C for 2 minutes, a 2nd PAB at 95 °C for 6 minutes, a 1st PEB at 65 °C for 2 minutes, a 2nd PEB at 95 °C for 6 minutes, and development for 10 minutes [9].

Figure 6 shows simulation results of the embedded micro channels for various cross-sectional shapes on the mask-movement trajectory. The simulation results of a negative CAR are aerial images of the illumination calculation and the inverse approach in Fig. 6(a), the PAG concentration of Eq. (3) after the exposure process in Fig. 6(b), the cross-linked polymer concentration of Eq. (8) after PEB in Fig. 6(c), the dissolution rate concentration of Mack's model for development in Fig. 6(d), and pattern profiles of the ray trace algorithm in Figs. 6(f), (h) and (j). The aerial image without a moving mask is modified into the deposited dose with a moving mask by using the inverse approach with the conversion step in Fig. 4. Various channel shapes correspond to various aerial images. The simulation results in Figs. 6(f), (h), and (j) are in good agreement with the experimental micro channel results for 30-, 50-, and 100-μm movement ranges of the mask in Figs. 6(e), (g), and

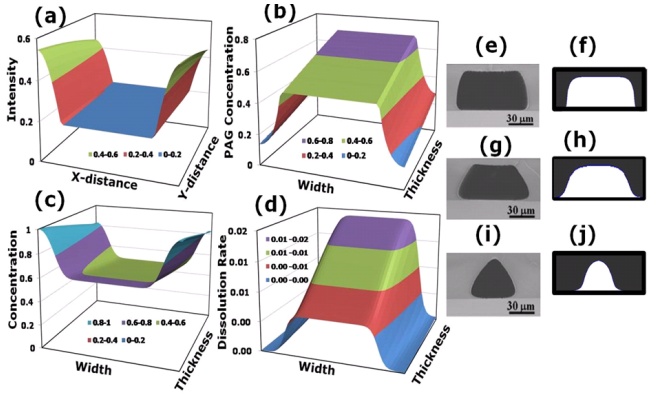

Fig. 6. Comparison of simulation results with experiment results in negative CAR processes for an embedded micro channels: (a) aerial image, (b) PAG concentration, (c) cross-linked polymer concentration, (d) development rate concentration, (e), (g), and (i) experimental results [10, 11], and (f), (h), and (j) simulation results.

(i), respectively. Experiment conditions corresponding to simulation conditions were a 100-μm pattern width, a 10-μm pitch, a 1-μm space width for the mask pattern, a 150-mJ/cm^2 incident dose, a 50-μm resist thickness, a 1st PEB at 65 °C for 1 minutes, a 2nd PEB at 95 °C for 4 minutes, and development for 8 minutes [10, 11]. Although the comparison of the simulation results with the experimental results for embedded-nano-channels is not shown because of the absence of experimental data, a simulation of the channels is possible in terms of the simulation results for the nano L/S pattern in Fig. 5.

The aerial image with a moving-mask is different from the aerial image without a moving-mask. In this paper, a direct simulation of aerial images due to the moving-mask technology is not considered. The aerial image without a moving-mask is calculated and is approximately modified into the deposited dose inside a resist with a moving mask. For this description, Fig. 3 shows the dose deposited inside a resist transferred from the mask pattern due to a moving mask. Figure 4 shows deposited dose which was extracted from a SEM image of the experiment data by using an inverse method.

V. CONCLUSION

Moving-mask lithography can serve as a high precise 3D micro/nano fabrication method because the 3D photoresist microstructure can be defined by using the moving-mask trajectory. Various 3D micro channel formations in thick/thin negative-tone photoresists were modeled and simulated. To establish confidence in modeling and simulation, we compared the thick/thin line and space patterns and the various shapes of the micro-embedded channels with those of experiments. Simulated results matched the experimental results well. The accomplishment and the improvement of the moving-mask technology can yield not only an effective way to minimize time and cost for 3D microstructuring but also a basic way to study both optics and resist materials.

ACKNOWLEDGMENTS

This research was supported by Basic Science Research Program through the National Research Foundation on Korea (NRF) funded by the Ministry of Education, Science and Technology (2009-0074676).

REFERENCES

[1] W. D. Volkmuth and R. H. Austin, Nature **358**, 600 (1992).
[2] Y. Hirai, Y. Inamoto, K. Sugano, T. Tsuchiya and O. Tabata, J. Micromech. Microeng. **17**, 199 (2007).
[3] Y. Hirai, S. Hafizovic, N. Matsuzuka, J. G. Korvink and O. Tabata, J. Microelectromech. Syst. **15**, 1, 159 (2006).
[4] S.-K. Kim and H.-K. Oh, J. Korean Phys. Soc. **51**, 4, 1413 (2007).
[5] S.-K. Kim, J. Korean Phys. Soc. **49**, 3, 1211 (2006).
[6] S.-K. Kim, H.-K. Oh, Y.-D. Jung and I. An, Jpn. J. Appl. Phys. **47**, 11, 8333 (2008).
[7] S.-K. Kim, H.-K. Oh, Y.-D. Jung and I. An, J. Korean Phys. Soc. **55**, 2, 661 (2009).
[8] K. Patel, M. Lawson, P. Varanasia, D. Medeirosb, G. Wallraff, P. Brock, R. DiPietroc, Y. Nishimura, T. Chibad and M. Slezake, Proc. SPIE **5376**, 536874 (2004).
[9] Y. Sensu, A. Sekiguchi, S. Mori and N. Honda, Proc. SPIE **5753**, 1170 (2005).
[10] Y. Inamoto, Y. Hirai, K. Sugano, T. Tsuchiya and O. Tabata, The 7th International Workshop on High Aspect Ratio Micro Structure Technology (HARMST2007, Besancon, France, June 2007), p. 31.
[11] Y. Hirai, K. Sugano, T. Tsuchiya, O. Tabata, in The 17th International Conference on Solid-State Sensors, Actuators and Microsystems (Transducers'09, Denver, United States, Jun. 21-25, 2009), p. 1616.